Journal of Power Sources 195 (2010) 402–411

Contents lists available at ScienceDirect

Journal of Power Sources

journal homepage: www.elsevier.com/locate/jpowsour

# A comprehensive evaluation of a Ni–$Al_2O_3$ catalyst as a functional layer of solid-oxide fuel cell anode

Wei Wang, Chao Su, Yuzhou Wu, Ran Ran, Zongping Shao *

*State Key Laboratory of Materials-Oriented Chemical Engineering, College of Chemistry & Chemical Engineering, Nanjing University of Technology, No. 5 Xin Mofan Road, Nanjing, 210009, PR China*

ARTICLE INFO

*Article history:*
Received 29 May 2009
Received in revised form 30 July 2009
Accepted 30 July 2009
Available online 8 August 2009

*Keywords:*
Solid-oxide fuel cells
Nickel–alumina
Catalyst layer
Methane
Carbon deposition

ABSTRACT

An inexpensive 7 wt.% Ni–$Al_2O_3$ composite is synthesized by a glycine–nitrate process and systematically investigated as anode catalyst layer of solid-oxide fuel cells operating on methane fuel by examining its catalytic activity towards methane partial oxidation, steam and $CO_2$ reforming at 600–850 °C, cell performance, mechanical performance, and carbon deposition properties. Ni–$Al_2O_3$ shows comparable catalytic activities to Ru–$CeO_2$ for the above three reactions. The cell with a Ni–$Al_2O_3$ catalyst layer delivers maximum peak power densities of 494 and 532 mW $cm^{-2}$ at 850 °C, operating on methane–$H_2O$ and methane–$CO_2$ mixture gases, respectively, which are comparable to those operating on hydrogen. Ni–$Al_2O_3$ is found to have better mechanical performance than Ru–$CeO_2$. $O_2$-TPO demonstrates that Ni–$Al_2O_3$ does not inhibit the carbon formation under pure methane atmosphere, while the introduction of steam or $CO_2$ can effectively suppress coke formation. However, due to the low nickel content in the catalyst layer, the coke formation over the catalyst layer is actually not serious under real cell operation conditions. More importantly, Ni–$Al_2O_3$ effectively protects the anode layer by greatly suppressing carbon formation over the anode layer, especially near the anode–electrolyte interface. Ni–$Al_2O_3$ is highly promising as an anode functional layer for solid-oxide fuel cells.



## 1. Introduction

Recently, there has been tremendous interest in fuel cells as electrical power generators because of their high energy-conversion efficiency, low emissions, and size flexibility, with capacities ranging from several milliwatts to the megawatts level [1–3]. Among the many types of fuel cells, solid-oxide fuel cells (SOFCs) have attracted particular attention because of their fuel flexibility [4,5]. Besides hydrogen, hydrocarbons, carbon monoxide, ammonia, alcohols, and solid carbon can all be used as potential fuels [6–12]. This feature is very attractive for near-future applications since the public infrastructure for hydrogen production, storage and transportation is still far from mature, while hydrocarbons are currently widely available. Actually, hydrogen is presently produced mainly by steam reforming of hydrocarbons.

When hydrocarbons are adopted as the fuels for SOFCs, they are typically first externally reformed to $CO + H_2$ before being introduced into the fuel cell reactor [13,14]. The external reforming process, however, not only reduces the overall energy-conversion efficiency, but also produces additional greenhouse gases. Because of this, direct hydrocarbon-fueled SOFCs have been gaining more and more attention recently [15–18]. As the simplest hydrocarbon, methane is the main component in the huge reserves of natural gas and coal-bed gas, and also the renewable resource of biogas. In principle, the simplest way to operate an SOFC on methane fuel is direct electro-catalytic oxidation of methane over the anode. However, the state-of-the-art sintered nickel-cermet anode catalyzes the $CH_4$ decomposition reaction that easily causes coke formation over the nickel catalyst surface and consequently, fast deterioration of the cell performance [19,20]. The development of novel anode materials with high coking-resistant capabilities has been extensively explored. Among them, $CeO_2$–Cu cermet anodes and perovskite-type $La_{1-x}Sr_xCr_{1-y}Mn_yO_3$ oxide anodes have shown high resistance towards coke formation [21–24]. However, such anodes always show poor electrochemical activity for methane oxidation and consequently, poor cell performance was obtained [21–24]. Development of new anode materials with high electro-catalytic activity for methane oxidation but not for the methane cracking reaction is the key to realizing direct-methane SOFCs.

An alternative way to operate on methane fuel is to integrate the catalytic conversion of methane to syngas reaction (i.e., partial oxidation, steam reforming or $CO_2$ reforming) with SOFCs internally [25–29]. Since CO and $H_2$ have much higher electrochemical activity than methane, such an operating mode can effectively improve the cell performance when using methane fuel. Furthermore, it can also effectively suppress carbon deposition over the

* Corresponding author. Tel.: +86 25 83172256; fax: +86 25 83172256.
*E-mail address:* shaozp@njut.edu.cn (Z. Shao).

0378-7753/$ – see front matter © 2009 Elsevier B.V. All rights reserved.
doi:10.1016/j.jpowsour.2009.07.053

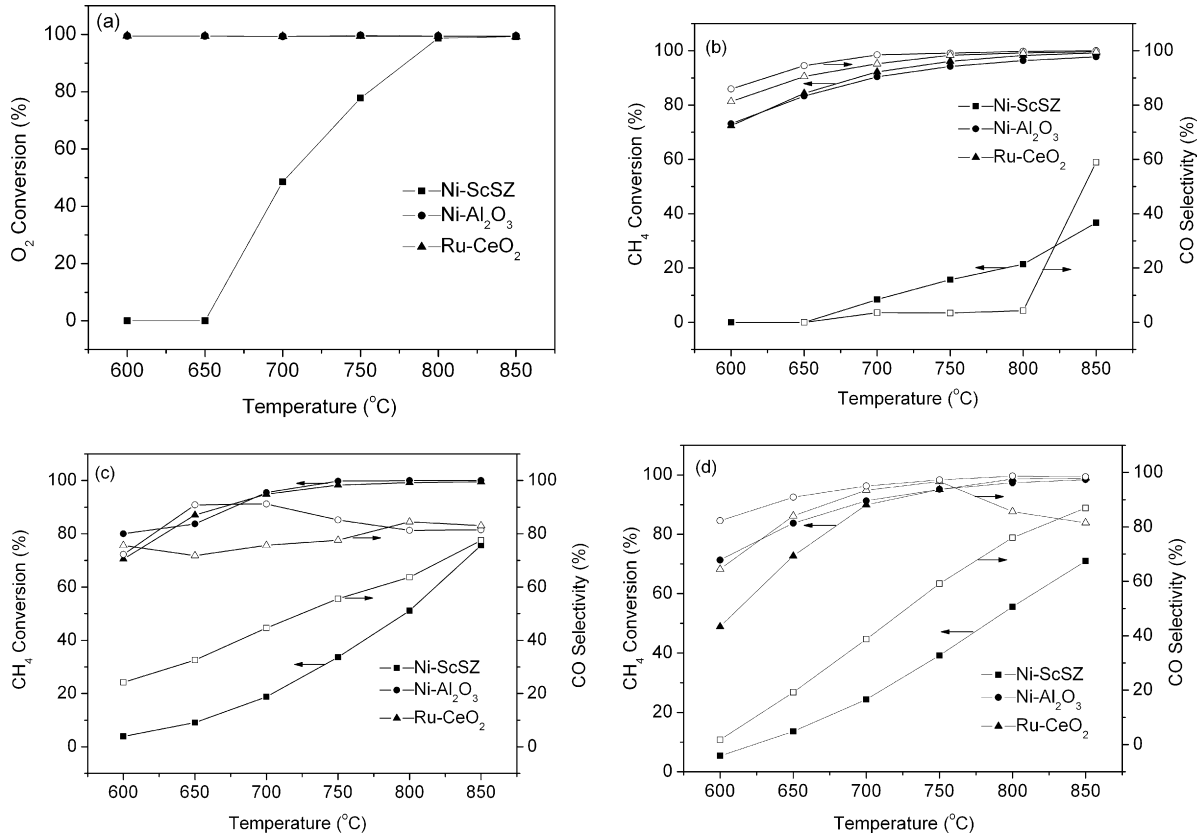


**Fig. 1.** Catalytic activity of Ni–$Al_2O_3$, Ru–$CeO_2$ and Ni–ScSZ catalysts for (a and b) partial oxidation ($CH_4$:$O_2$ = 2:1), (c) steam reforming ($CH_4$:$H_2O$ = 1:1) and (d) $CO_2$ reforming ($CH_4$:$CO_2$ = 1:1).

anode surface. However, the traditional Ni-cermet anodes usually show poor catalytic activity towards the above reactions, especially at reduced temperatures. Very recently, the deposition of a highly active catalyst layer over the anode surface was found to be an effective way of increasing the cell performance when operating on hydrocarbon fuels [30–33]. It not only increases the cell power output, but also obviously suppresses the coke formation over the anode surface. In particular, Ru–$CeO_2$ has been found to be an efficient catalyst for operating on methane, propane and butane fuels, in both single-chamber and dual-chamber cell configurations [30,32–36]. However, the high price of Ru–$CeO_2$ is the main obstacle towards its large-scale application. The development of cheap and highly active materials for the functional layer is then critical.

In our previous communication, we demonstrated that an inexpensive Ni–$Al_2O_3$ catalyst also had very high catalytic activity towards methane partial oxidation, methane steam reforming and methane $CO_2$ reforming reactions at 750–850 °C [31]. The cell with the Ni–$Al_2O_3$ catalyst layer showed significant improvement in cell performance, operating on both pure methane and methane–oxygen mixtures of gases. Furthermore, the cell performance deterioration rate was also greatly reduced even when operating on pure methane fuel.

In this paper, we present a comprehensive investigation of Ni–$Al_2O_3$ as the catalyst layer of SOFC anode operating on methane–oxygen, methane–$H_2O$, and methane–$CO_2$ gas mixtures. The following characterizations were investigated: catalytic activity for syngas production from methane–oxygen, methane–$CO_2$ and methane–$H_2O$ mixture gases, cell performance, mechanical performance of the catalyst layer under repeated thermal and redox cycling, and coke deposition properties. A comparative study with Ru–$CeO_2$ catalyst was also conducted.

## 2. Experimental

### 2.1. Catalyst powder synthesis and cell fabrication

Both 7 wt.% Ni–$Al_2O_3$ and 7 wt.% Ru–$CeO_2$ powders, investigated as the materials for the catalyst layer, were synthesized by a glycine nitrite process (GNP) [37]. Taking the synthesis of Ni–$Al_2O_3$ as an example, stoichiometric amounts of nickel nitrate and alumina nitrate were first dissolved in de-ionized water, glycine was then added at a molar ratio of 2.0 between the glycine and total metallic cations. The water in the solution was then evaporated by heating over a hot plate under stirring to create a liquid precursor, which was then moved to an electrical oven at 240 °C to induce auto-combustion. The primary powder was further calcined at 850 °C for 5 h in static air.

The fuel cell materials, including the cathode $La_{0.8}Sr_{0.2}MnO_3$ (LSM) and the electrolyte $(Sc_2O_3)_{0.1}(ZrO_2)_{0.9}$ (ScSZ), were prepared by an EDTA–citrate complexing process [38,39]. The fuel cell adopted in this study was a 60 wt.% NiO + 40 wt.% ScSZ anode-supported thin-film ScSZ electrolyte fuel cell (~20 μm), fabricated by a dual dry-pressing/sintering process [39]. Ni–ScSZ anode powder was first pressed into a substrate disk using a stainless steel die under a pressure of 120 MPa. ScSZ powder was distributed over the anode surface homogenously and followed by a second press under a pressure of 240 MPa to form the green dual layer cell, which was then sintered at 1500 °C for 5 h to densify the electrolyte layer. The sintered cells had a diameter of ~13 mm and a thickness of ~0.3 mm.

### 2.2. Catalytic evaluation

The catalytic activity of the catalysts and anode material was studied in a flow-through type fixed-bed quartz-tube reactor with

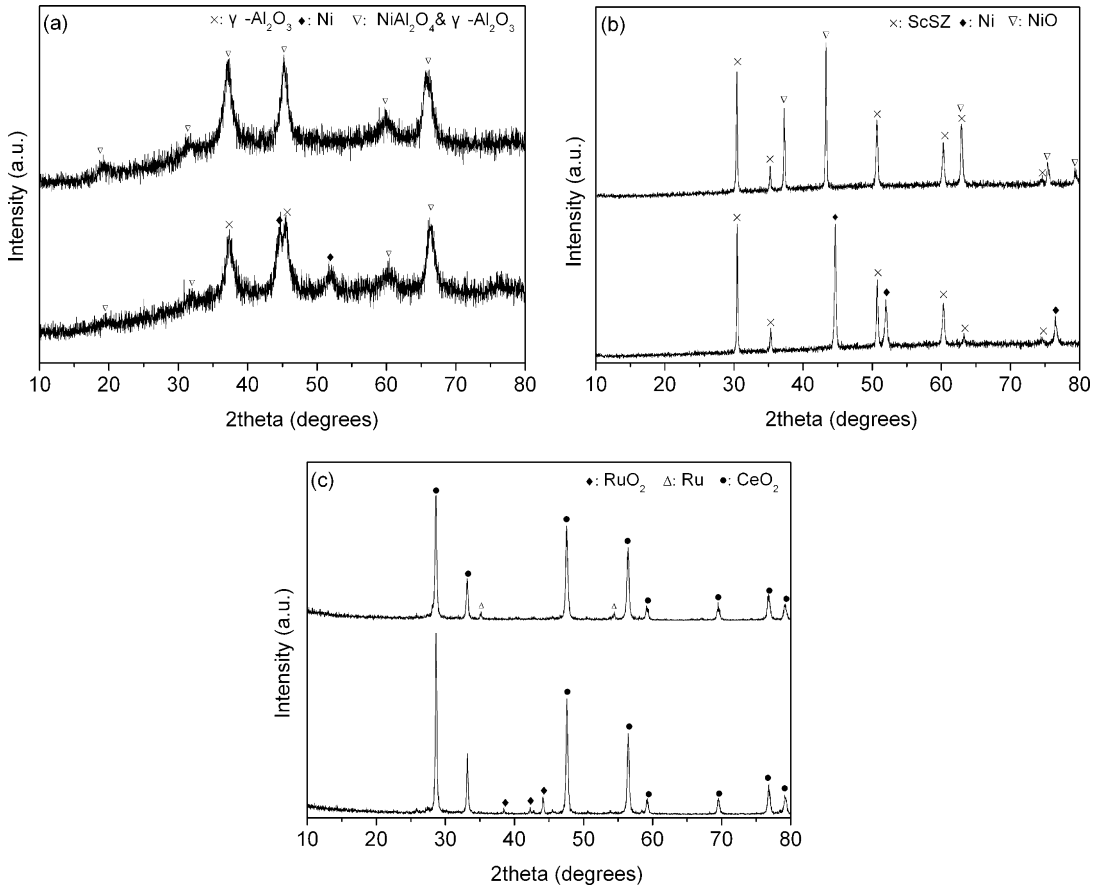


**Fig. 2.** XRD patterns of the Ni–$Al_2O_3$ (a), Ni–ScSZ (b) and Ru–$CeO_2$ (c) catalysts before and after the hydrogen reduction.

an inner diameter of ~8 mm. About 0.2 g of catalyst particles in the size range of 60–80 mesh was dropped into the middle of the reactor. The gas flow for partial oxidation, steam reforming and $CO_2$ reforming reactions were precisely controlled by AFC 80MD digital mass flow controllers (Qualiflow). The gas mixtures were introduced from the top of the reactor, and the effluent gases from the bottom of the reactor were introduced to a Varian 3800 gas chromatograph, equipped with Hayesep Q, Poraplot Q and 5 Å molecular sieve capillary columns for the separation of $H_2$, $O_2$, CO, $CO_2$ and $CH_4$. Helium was used as the carrier gas. Typically, the methane flow rate was kept at 10 ml $min^{-1}$ [STP] and the diluting helium gas at 80 ml $min^{-1}$ [STP].

### 2.3. Characterization techniques

The phase structure of synthesized powders was characterized by an X-ray diffractometer (XRD, ARL X' TRA) equipped with Cu Kα radiation (λ = 0.1541 nm). The cross-sectional morphologies of the fuel cells were examined using an environmental scanning electron microscope (ESEM, QUANTA-2000) equipped with an EDX detector (QUANTA-200,132-10).

Hydrogen temperature-programmed reduction ($H_2$-TPR) was performed to identify the interaction between NiO and the support. Approximately 0.03 g of oxide powder was placed in a U-type quartz reactor with an inner diameter of ~3 mm. The sample was pretreated under a pure argon atmosphere at the flow rate of 30 ml $min^{-1}$ for 30 min. After cooling down to room temperature, the atmosphere was switched to 10 vol.% $H_2$/Ar, and the reactor was programmatically heated to 930 °C at 10 °C $min^{-1}$. The consumption of hydrogen was monitored by an in situ thermal conductivity detector (TCD) detector using a BELCAT-A apparatus.

For the carbon deposition tests, about 0.2 g samples were first placed in a flow-through type quartz-tube reactor and treated at high temperature (typically 850 °C) under a methane-containing atmosphere at the flow rate of 40 ml $min^{-1}$ for 5 min. The catalysts were then cooled to room temperature under an inert atmosphere (nitrogen or argon). After the treatment, approximately 0.05 g of powder was placed into a U-type quartz reactor with an inner diameter of ~3 mm. Pure oxygen (for oxygen temperature-programmed oxidization, $O_2$-TPO) at the flow rate of 20 ml $min^{-1}$ [STP] was then introduced from the top of the reactor. After flowing with the gas at room temperature for ~30 min, the reactor was programmatically heated to 800 °C at 10 °C $min^{-1}$. The deposited solid carbon over the catalyst surface was progressively oxidized into gaseous $CO_2$. The effluent gas from the reactor was connected with a Hiden QIC-20 Mass spectroscope (MS) for in situ monitoring of concentration variation of the $CO_2$.

The *I–V* polarization of the cells was measured at 750–850 °C using a Keithley 2420 source meter in 4-probe mode. During the measurement, methane fuel or a mixture of $CH_4$–$O_2$, $CH_4$–$CO_2$ or $CH_4$–$H_2O$ was fed into the anode chamber at a flow rate of 40 ml $min^{-1}$ [STP] while ambient air was provided as the oxidant gas at in the cathode chamber.

## 3. Results and discussion

### 3.1. Catalytic activity

Presently, there is considerable interest in reducing the traditional 1000 °C operating temperature of SOFCs to the intermediate-temperature range of 600–850 °C because of the many benefits associated with such a reduction [40]. When the fuel

cell is integrated with the methane internal reforming or partial oxidation reactions, it places much stricter requirement on the catalyst layer. Our primary investigations demonstrated that Ni–$Al_2O_3$ catalyst possessed very high activity for methane partial oxidation (Eq. (1)), methane steam reforming (Eq. (2)), and methane $CO_2$ reforming (Eq. (3)) between 750 and 850 °C [31].

$$CH_4 + 1/2O_2 = CO + 2H_2 \quad (1)$$

$$CH_4 + H_2O = CO + 3H_2 \quad (2)$$

$$CH_4 + CO_2 = 2CO + 2H_2 \quad (3)$$

The catalytic activity of the combustion-synthesized Ni–$Al_2O_3$ for the above three reactions was further comparatively studied with combustion-synthesized 7 wt.% Ru–$CeO_2$ and Ni–ScSZ anode material over the intermediate-temperature range 600–850 °C. During the fuel cell fabrication, the catalyst layer was fired onto the anode surface at 850 °C while the Ni–ScSZ anode was sintered at 1500 °C, together with the electrolyte layer. The Ni–$Al_2O_3$, Ru–$CeO_2$ and Ni–ScSZ catalysts were calcined at 850, 850 and 1500 °C for 5 h, respectively. Fig. 1 shows the oxygen conversion, methane conversion and CO selectivity over Ni–$Al_2O_3$, Ru–$CeO_2$ and Ni–ScSZ catalysts for the above three reactions at the methane to oxygen/$H_2O$/$CO_2$ ratios of 2:1, 1:1 and 1:1, respectively. Over the whole investigated temperature range from 600 to 850 °C, Ni–$Al_2O_3$ showed similar catalytic activity to Ru–$CeO_2$ catalyst, but was considerably higher than that of Ni–ScSZ, for all three above reactions. When operating on methane–oxygen gas mixtures, 100% oxygen conversion was achieved for both Ni–$Al_2O_3$ and Ru–$CeO_2$ catalysts over the entire temperature range under investigation, while oxygen conversion was only 48.6% for the Ni–ScSZ catalyst (Fig. 1a), even at 700 °C. At 600 °C, the $CH_4$ conversion reached 73.1, 80.0, and 71.3% for reactions (1)–(3), respectively, when using the Ni–$Al_2O_3$ catalyst. They were 0.0, 3.9, and 5.4% for the Ni–ScSZ catalyst. The above results further suggest Ni–$Al_2O_3$ as the catalyst layer of choice for IT-SOFCs from the aspect of catalytic activity for methane conversion to syngas.

It is well known that the activity of nickel-based catalysts for methane partial oxidation is closely related with the interaction of the nickel with the support [41]. Fig. 2 shows the XRD patterns of the Ni–$Al_2O_3$, Ni–ScSZ and Ru–$CeO_2$ catalysts before and after the hydrogen reduction. Before the reduction, both Ni–ScSZ and Ru–$CeO_2$ catalysts displayed a physical mixture of their respective components (NiO and ScSZ for NiO–ScSZ, and $RuO_2$ and $CeO_2$ for $RuO_2$–$CeO_2$), while the Ni–$Al_2O_3$ catalyst was composed of a spinel-type phase and γ-$Al_2O_3$ with no NiO detected. This suggests NiO and γ-$Al_2O_3$ reacted to form a new $NiAl_2O_4$ spinel in the Ni–$Al_2O_3$ catalyst. Fig. 3 shows the $H_2$-TPR of the Ni–$Al_2O_3$ and Ni–ScSZ catalysts. It has been reported that the reduction temperature of NiO in $H_2$ was about 330 °C for free NiO or NiO species with very weak interactions with the support phase [42]. Only one reduction peak at around 830 °C was observed for the Ni–$Al_2O_3$ catalyst, which was attributed to the reduction of $NiAl_2O_4$ spinel to metallic nickel and $Al_2O_3$. It is interesting that strong and complicated interactions also existed between NiO and ScSZ based on the $H_2$-TPR results. The $H_2$-TPR profile of NiO–ScSZ can be divided into six overlapped reduction peaks with peak temperatures of 510, 563, 663, 710, 770 and 841 °C. Therefore, at least six different types of interactions, with different strengths, existed between the NiO and ScSZ phases. Such interactions are unlikely from the formation of new solid solutions, since the XRD patterns of the composite just displayed a physical mixture of NiO and ScSZ phases. Another important factor in determining the catalytic activity of nickel is its crystalline size. The crystalline size of the metallic nickel in Ni–$Al_2O_3$ and Ni–ScSZ was 6.7 and 25.7 nm, respectively, calculated from the XRD diffraction peak at $2\theta = 51.8°$ using the Scherrer equation. The strong interaction of NiO species with the support phase,

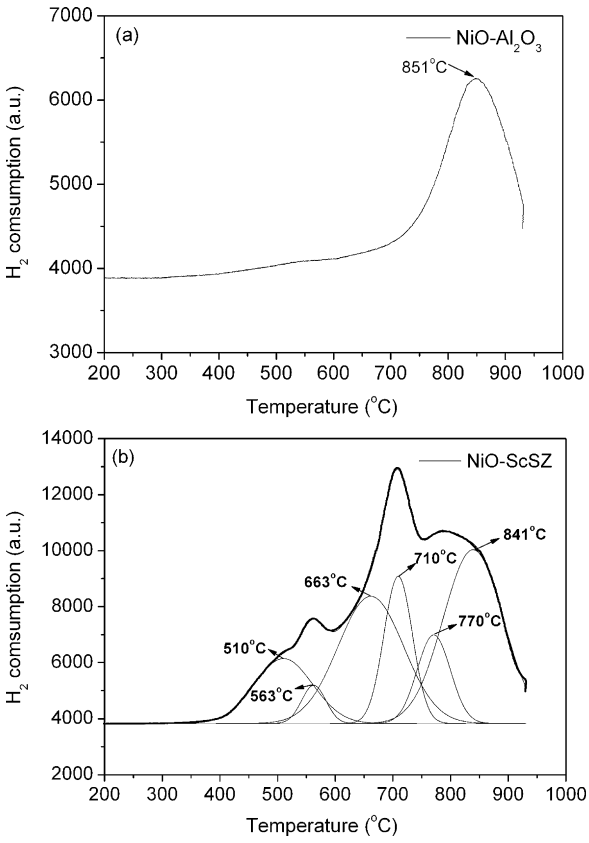


**Fig. 3.** Profiles of $H_2$ temperature-programmed reduction of (a) Ni–$Al_2O_3$ and (b) Ni–ScSZ.

as evidenced by the $H_2$-TPR and powder XRD, and relatively low calcination temperature contributed much to the fine crystalline size of the nickel in Ni–$Al_2O_3$ catalyst, while the large grain size of the nickel in Ni–ScSZ was due to the ultra-high sintering temperature (1500 °C). The relatively poor activity of Ni–ScSZ for methane conversion was likely associated with the large crystalline size from the ultra-high temperature sintering.

It has been reported that metallic nickel also has a certain type of interaction with $Al_2O_3$ support, which can suppress the crystalline growth and ensure long-term operational stability [43]. The operational stability of Ni–$Al_2O_3$ catalyst was selectively investigated for methane partial oxidation at a methane to oxygen ratio of 4:1, which has turned out to be the optimal ratio to achieve

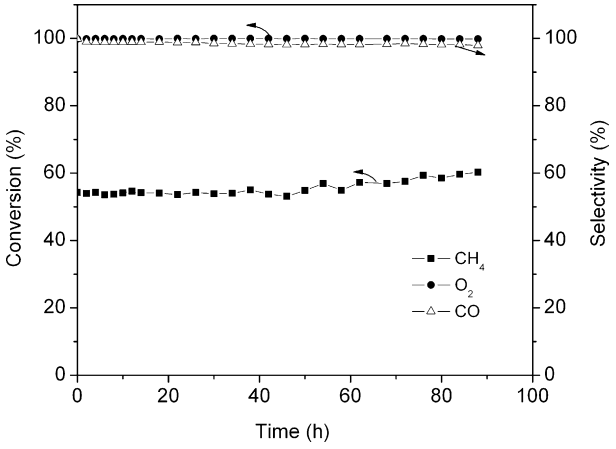


**Fig. 4.** The time dependence of methane conversion and selectivity to CO under the reaction conditions ($CH_4$:$O_2$ = 4:1, Ni–$Al_2O_3$ catalyst).

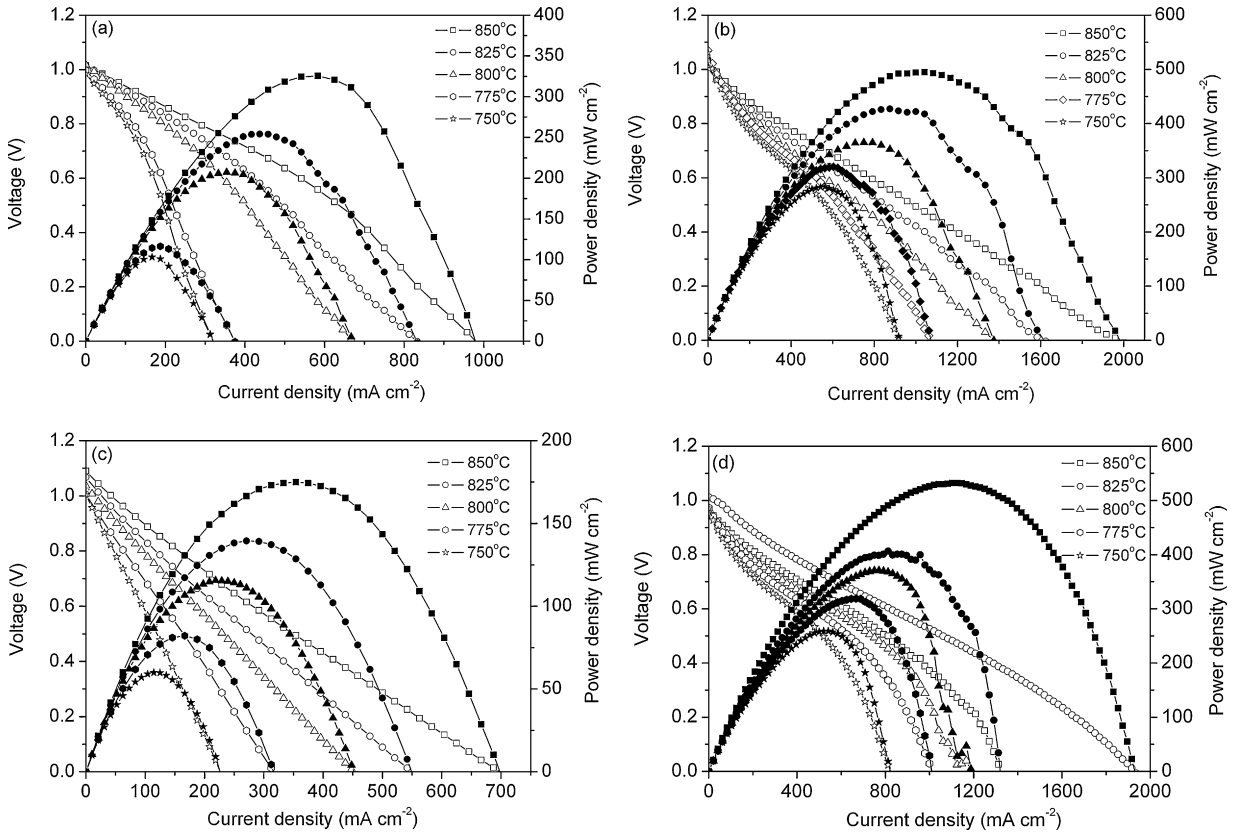


**Fig. 5.** The *I–V* and *I–P* curves of the fuel cells without and with the Ni–$Al_2O_3$ catalyst layer operating on a mixed gas composed of 66.7% $CH_4$ mixed with 33.3% $H_2O$ (a and b) and 66.7% $CH_4$ mixed with 33.3% $CO_2$ (c and d) at different temperatures.

the maximum power output for the SOFC when operating on methane–oxygen mixture gases [31]. As shown in Fig. 4, during the 90 h of operation, the methane conversion and CO selectivity was fairly stable, suggesting the catalyst indeed has good resistance to sintering.

### 3.2. Cell performance

Previously, we reported that the cell performance was obviously improved by adopting Ni–$Al_2O_3$ as an anode functional layer when operating both on pure methane and methane–oxygen gas mixtures [31]. The improved cell performance is due to the increased catalytic activity of the anode towards methane partial oxidation, which results in an increased hydrogen concentration in the anode atmosphere. The much higher catalytic activity of Ni–$Al_2O_3$ for methane steam reforming and $CO_2$ reforming than the Ni–ScSZ anode suggests the cell performance should also be improved when operating on methane–$H_2O$ or methane–$CO_2$ gas mixtures by adopting a Ni–$Al_2O_3$ anode catalyst layer. In other words, Ni–$Al_2O_3$ should also be an ideal catalyst for internal reforming of methane fuel too. The cell performance while operating on methane–steam gas mixtures and methane–$CO_2$ gas mixtures gases with $CH_4$ to $H_2O$ and $CH_4$ to $CO_2$ ratios of 2:1 were then tested. Shown in Fig. 5 are the *I–V* and *I–P* curves of the fuel cells without and with the Ni–$Al_2O_3$ catalyst layer at different temperatures. When no catalyst layer was deposited over the anode, the cell delivered peak power densities of 324, 254, 207, 116 and 103 mW $cm^{-2}$ at 850, 825, 800, 775 and 750 °C, operating on methane-steam gas mixtures respectively, while they increased to 494, 427, 365, 320, and 282 mW $cm^{-2}$ when a Ni–$Al_2O_3$ catalyst layer was applied. Similarly, they were 175 mW $cm^{-2}$ (850 °C), 139 mW $cm^{-2}$ (825 °C), 115 mW $cm^{-2}$ (800 °C), 82 mW $cm^{-2}$ (775 °C) and 60 mW $cm^{-2}$ (750 °C) when operating on methane–$CO_2$ mixture, and they increased to 532, 406, 370, 318 and 259 mW $cm^{-2}$ for the cell with the catalyst layer.

Table 1 lists the peak power densities (PPDs) at 850 °C of the fuel cells with and without the Ni–$Al_2O_3$ anode catalyst layer operating on methane–$H_2O$ or methane–$CO_2$ gas mixtures at various methane to steam/$CO_2$ ratios. For completeness, the cell performance operating on methane–oxygen gas mixtures is also presented [31]. It was found that the PPDs of the cells operating on all three gas mixtures first increased with the increase of methane to oxygen/steam/$CO_2$ ratios, and then decreased. At all ratios, the cell with the catalyst layer had higher PPDs than those of the cells with a bare Ni–ScSZ anode. The maximum PPDs for the cell with the catalyst layer were 456, 494 and 532 mW $cm^{-2}$, when operating on methane–oxygen, methane–$H_2O$ and methane–$CO_2$ gas mixtures, respectively, which were reached at methane to oxygen/$H_2O$/$CO_2$ ratios of 4:1, 2:1 and 2:1, respectively. For the cell without the anode catalyst layer, the maximum PPDs were

**Table 1**
Peak power density (PPD) of the fuel cells with and without Ni–$Al_2O_3$ catalyst layer at 850 °C operating on methane fuel with various methane to $O_2$/$H_2O$/$CO_2$ ratios.

| $CH_4$% (balanced by $O_2$) | 100 | 88.9 | 80 | 66.7 | 0 (pure $H_2$) |
|---|---|---|---|---|---|
| PPD (mW $cm^{-2}$) | | | | | |
| Without catalyst layer | 152 | 242 | 231.5 | 199 | 545 |
| With catalyst layer | 382 | 408 | 456 | 386 | 660 |
| $CH_4$% (balanced by $H_2O$) | 100 | 80 | 66.7 | 50 | 0 (pure $H_2$) |
| PPD (mW $cm^{-2}$) | | | | | |
| Without catalyst layer | 152 | 234 | 324 | 234 | 545 |
| With catalyst layer | 382 | 404 | 493 | 429 | 660 |
| $CH_4$% (balanced by $CO_2$) | 100 | 80 | 66.7 | 50 | 0 (pure $H_2$) |
| PPD (mW $cm^{-2}$) | | | | | |
| Without catalyst layer | 152 | 261 | 175 | 193 | 545 |
| With catalyst layer | 382 | 460 | 532 | 431 | 660 |

242, 324 and 262 mW cm$^{-2}$ for methane–oxygen, methane–$H_2O$ and methane–$CO_2$, respectively, which were reached at methane to oxygen/$H_2O$/$CO_2$ ratios of 8:1, 2:1 and 4:1, respectively.

In a previous study, Jiang and Virkar demonstrated that the performance of SOFC operating on $H_2$ and CO gas mixtures was very high [44]. For a fuel gas containing greater than 50% $H_2$ (and balanced by CO), it was argued that $H_2O$ produced by the electrochemical oxidation of $H_2$ was more than sufficient to react with CO present to form $H_2$ and $CO_2$. In such a case, there should be little difference in performance when compared to pure $H_2$ as fuel. The above observations can well explain the small differences in maximum PPD obtained for the fuel cell with the catalyst layer when operating on methane–oxygen, methane–$H_2O$ and methane–$CO_2$ gas mixtures in this study, as demonstrated in Table 1.

Since methane has a much slower electrochemical oxidation rate than $H_2$ over nickel anodes, the maximum PPDs should be reached at the condition where methane was totally converted by the catalytic reaction to form $H_2$ and CO. Assuming free gas diffusion inside the anode layer, the maximum PPDs should be reached at the condition of 100% methane conversion, i.e., it should be reached at methane to oxygen, methane to $H_2O$ and methane to $CO_2$ ratios of 2:1, 1:1 and 1:1, respectively, when operating on methane and oxygen/steam/$CO_2$ gas mixtures. The higher-than-expected experimental ratios needed to obtain the maximum PPDs could be explained by the diffusion blocking effect of the catalyst layer [31], which resulted in the actual methane concentration within the anode layer being lower than that in the feed gas and made the gas ratio needed to shift to the higher ratio to obtain the maximum PPDs.

For a cell without the catalyst layer, a too-low methane to $O_2$/$H_2O$/$CO_2$ ratio would result in high concentrations of unconverted $O_2$, $H_2O$, $CO_2$ and methane due to the poor catalytic activity of the anode, which then diluted the $H_2$/CO fuels and resulted in a lowered $H_2$/CO concentration. A too-high methane to $O_2$/$H_2O$/$CO_2$ ratio would also result in lowered $H_2$ and CO concentrations due to insufficient $H_2$/CO production. The maximum PPD was reached at the highest $H_2$ and CO concentration in the reforming gas, which was achieved at methane to $O_2$/$H_2O$/$CO_2$ ratios of 8:1, 2:1 and 4:1 when operating on methane–$O_2$, methane–$H_2O$ and methane–$CO_2$ gas mixtures, respectively, for the cell with a bare Ni–ScSZ anode, in this study.

### 3.3. Mechanical properties

In practical applications, fuel cells may experience repeated thermal and redox cycling, especially in portable application. The firm adhesion of the catalyst layer to the anode surface is critical for stable cell performance. The mechanical performance of the catalyst layer over the anode surface during the repeated redox cycling was investigated by $H_2$ reduction and $O_2$ oxidation at 850 °C for 20 cycles, while the thermal cycling stability of the catalyst layer was examined by repeated fast heating to 850 °C and then quenching to room temperature in air for 20 cycles. For comparison, the typical Ru–$CeO_2$ catalyst was also investigated in a similar way. Shown in Fig. 6 are the SEM images of

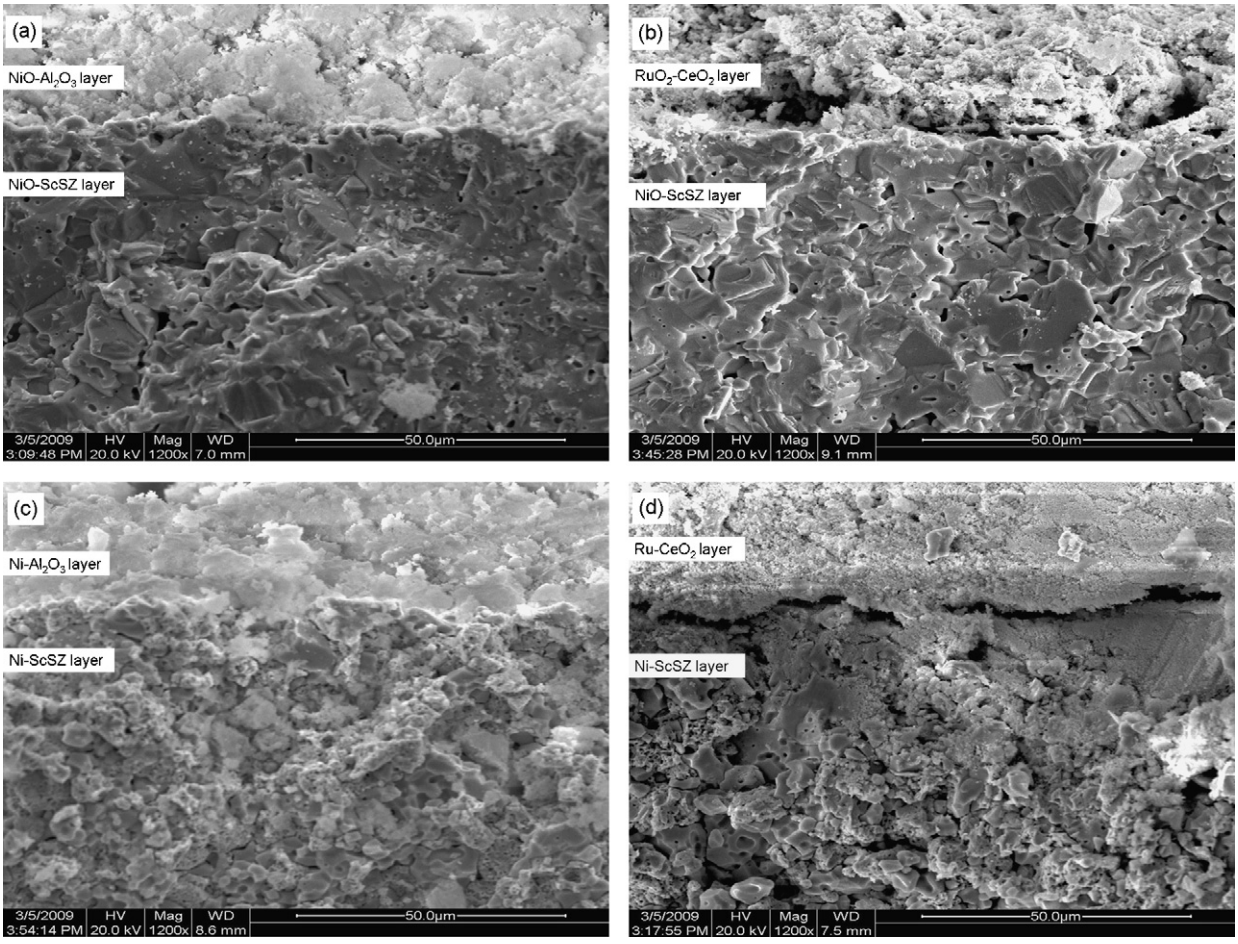


**Fig. 6.** The cross-sectional SEM pictures of the cells with the two different catalyst layers after the thermal cycling with Ni–$Al_2O_3$ catalyst layer (a) and with Ru–$CeO_2$ layer (b), and redox cycling with Ni–$Al_2O_3$ catalyst layer (c) and with Ru–$CeO_2$ layer (d).

the cells after the thermal cycling and redox cycling in cross-sectional view. When the Ni–$Al_2O_3$ was adopted as the catalyst layer, it still adhered to the anode surface very well after both the fast thermal cycling test and the redox cycling test. No delamination of the Ni–$Al_2O_3$ catalyst layer from the anode surface was observed by SEM over the entire cell. However, when Ru–$CeO_2$ catalyst was adopted as the catalyst layer, as shown in Fig. 6b and d, some cracks were formed between the catalyst and anode interface after both the thermal and redox cycling. The separation of the catalyst layer from the anode surface would eventually make the catalyst layer lose its functionality. This result suggests that Ni–$Al_2O_3$ is superior to Ru–$CeO_2$ in applications where repeated thermal cycling and redox cycling could be occurring, such as portable applications and single-chamber fuel cells application.

### 3.4. Carbon deposition

Rapid deterioration of the fuel cell performance was frequently observed with the nickel anode when operating on methane fuel, due to the coke formation over the anode surface that limits free gas adsorption and electrochemical oxidation of the fuel. Previously, we demonstrated that the cell stability was greatly improved by adopting a Ni–$Al_2O_3$ catalyst layer over the anode surface. It is well known that nickel-based catalysts catalyze carbon deposition. Acidic support also promotes such carbon formation [45]. The carbon deposition behavior of the Ni–$Al_2O_3$ catalyst was investigated by first treating it in pure methane at various temperatures at the flow rate of 40 ml $min^{-1}$ for 5 min, then protecting it with an inert gas at the flow rate of 40 ml $min^{-1}$ to room temperature, and finally conducting the temperature-programmed oxidation reaction. For comparison, the carbon deposition behavior of Ru–$CeO_2$ and Ni–ScSZ anode were also investigated.

Shown in Fig. 7 are the corresponding $O_2$-TPO profiles of the catalysts during the $O_2$-TPO process after treatment in pure methane for 5 min between 750 and 850 °C. The amount of active metal was ~3.5 mg for all three catalysts. It clearly shows that the Ru–$CeO_2$ had much superior coke resistance than the other two catalysts at all investigated temperatures. This is in good agreement with the literature results showing that Ru does not catalyze the methane cracking reaction. After treatment at 850 °C for 5 min, the absolute amount of coke formed over the Ru–$CeO_2$ catalyst was only about 6.34% of that over the Ni–$Al_2O_3$ catalyst, or 4.17% of that over the Ni–ScSZ catalyst. These results suggest that Ni–$Al_2O_3$ did not show an improvement in resistance towards coke formation as compared to Ni–ScSZ.

Shown in Fig. 8 are the $O_2$-TPO profiles of the Ni–$Al_2O_3$ catalyst after treatment in methane–$CO_2$ and methane–$H_2O$ gas mixtures at various ratios at 850 °C for a fixed time of 5 min. Methane was kept at 40 ml $min^{-1}$. It clearly demonstrates that the coke formation was greatly suppressed by introducing $CO_2$ or $H_2O$ into the methane fuel. The higher the $CO_2/H_2O$ to methane ratio, the less coke was formed. At a $CH_4$ to $H_2O/CO_2$ ratio of 2:1, negligible amounts of coke were formed over the Ni–$Al_2O_3$ catalyst, as evidenced by $CO_2$-TPD. It is interesting that the methane to $CO_2/H_2O$ ratio of 2:1 also resulted in the maximum cell performance when operating on methane–$CO_2$ and methane–$H_2O$ gas mixtures. The suppression of coke formation by introducing $CO_2$ and $H_2O$ can be explained by the following carbon elimination reactions:

$$C + CO_2 = 2CO \quad (4)$$

$$C + H_2O = CO + H_2, \quad (5)$$

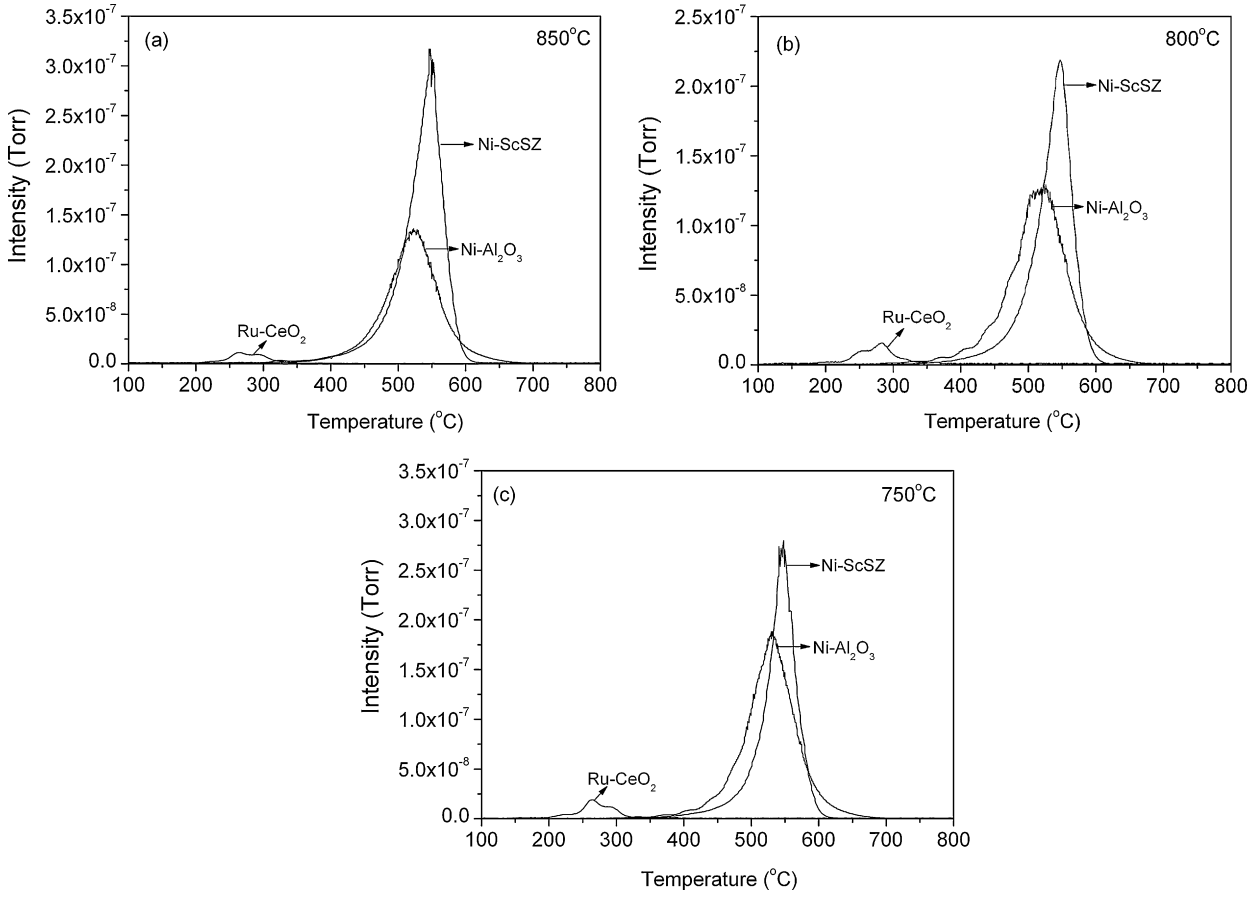


**Fig. 7.** $O_2$-TPO profiles of the three catalysts after treatment in pure methane for 5 min at 850 °C (a), 800 °C (b) and 750 °C (c).

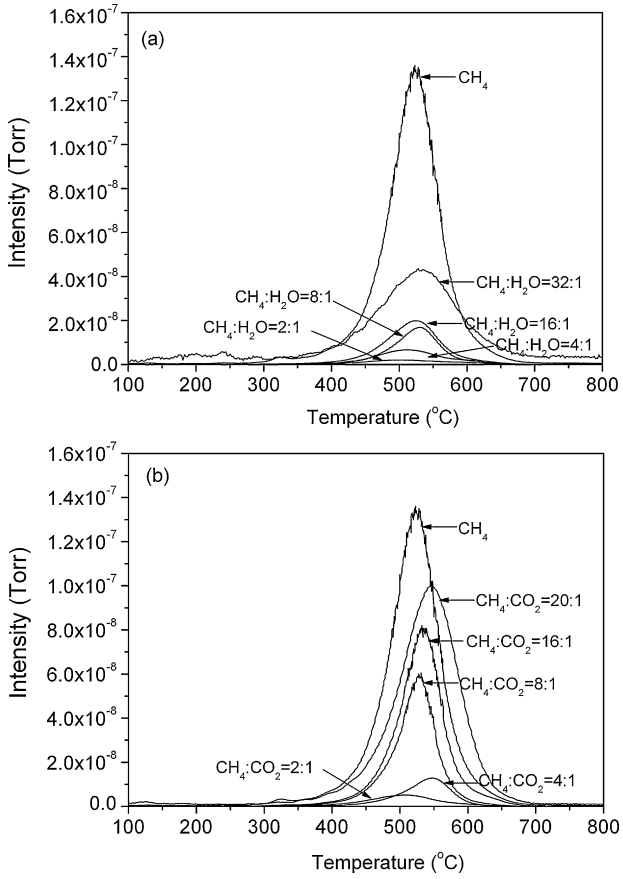


**Fig. 8.** $O_2$-TPO profiles of the Ni–$Al_2O_3$ catalyst after treatment in methane–$H_2O$ (a) and methane–$CO_2$ (b) gas mixtures with various ratios at 850 °C for a fixed time of 5 min.

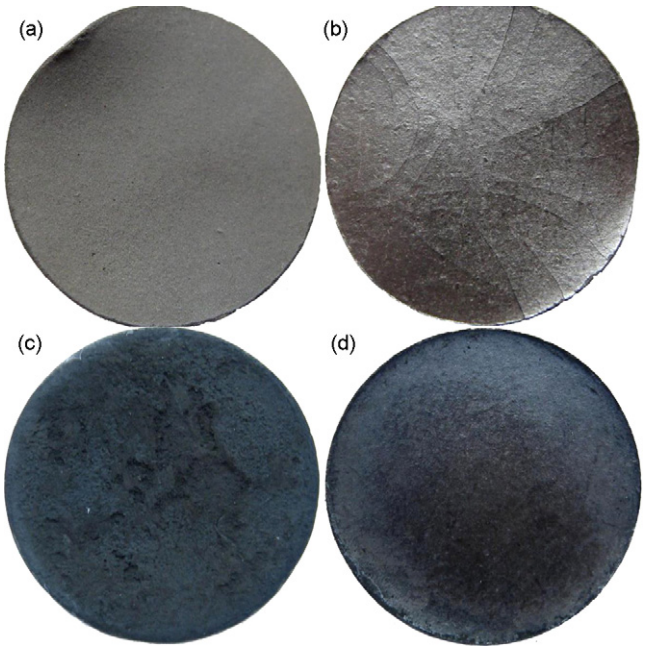


**Fig. 9.** Images of the fuel cell without (a and b) and with (c and d) the catalyst layer after treatment of pure methane for 5 min.

The above results suggest that Ni–$Al_2O_3$ is more promising as an internal reforming catalyst for operating on methane–$H_2O$ or methane–$CO_2$ gas mixtures than on pure methane fuel.

In our previous study we demonstrated that the cell operational stability was obviously improved by adopting the Ni–$Al_2O_3$ catalyst layer, even with pure methane as the fuel [31]. For example, the performance deterioration was about 43% after 90 min of operation with pure methane fuel at 850 °C for the cell with a bare Ni–ScSZ anode, while it was only 4% after 150 min of operation for a similar cell with a Ni–$Al_2O_3$ catalyst layer. To interpret such an improvement, a cell with the Ni–$Al_2O_3$ catalyst layer and a cell with a bare Ni–ScSZ anode were exposed to pure methane under open circuit voltage (OCV) condition at 850 °C for 10 min and then protected by an inert gas while cooling to room temperature in order to detect any morphological changes. It was observed by the unaided eye that the cell with the Ni–$Al_2O_3$ catalyst layer still retained perfect cell integrity. As for the cell with the bare nickel–ScSZ anode, it was distorted in some local regions and serious cracks had formed over the electrolyte surface, as shown in Fig. 9.

Carbon deposition over the anode was investigated by EDX at selected regions as shown in Fig. 10, i.e., within the ScSZ electrolyte (region 1), within the anode layer near the anode–electrolyte interface (region 2, about 20 μm from the anode–electrolyte interface), within the anode layer near the catalyst layer (region 3, about 20 μm from the catalyst–anode interface), and within the catalyst layer (region 4). For comparison, similar regions for a cell without the catalyst layer were also observed, named 1′, 2′, and 3′, respectively. As shown in Fig. 10e, f and g, a carbon peak of high intensity was detected at anode region 3′ for the cell without the catalyst layer. Even for region 2′ near the electrolyte–anode interface, a high carbon peak height was detected. For the cell with the catalyst layer, shown in Fig. 10a–d, the intensity of the carbon peak near the anode–electrolyte interface (region 2) was much smaller as compared to the similar region (2′) for the cell without the catalyst layer.

The samples for EDX examination were typically easily contaminated with carbon. In order to quantitatively analyze the carbon deposition from methane decomposition, carbon information over the freshly crashed ScSZ electrolyte was also obtained by EDX. Because of the dense electrolyte layer, there should be no carbon deposited over the cross-sectional region of the electrolyte from the methane decomposition. All the carbon detected by EDX over the electrolyte layer would then be contributed by contamination during the sample preparation for EDX measurement. Assuming the homogeneous distribution of the contaminated carbon over the whole sample prepared for EDX measurement, the amount of carbon deposited over the anode that was contributed by the methane thermal decomposition can be obtained by subtracting the contaminated carbon. At regions 2 and 3 for the cell with the catalyst layer, the actual carbon deposited was found to be $13.1 \pm 0.2$ and $22.4 \pm 0.2$ wt.%, respectively. Correspondingly, it was $24.9 \pm 0.1$ and $30.2 \pm 0.1$ wt.%, for the regions 2′ and 3′ for the cell without the catalyst layer. This clearly suggests that the catalyst layer protected the anode from carbon deposition, especially for the anode region near the anode–electrolyte interface.

It is well known that the electro-active zone of the anode is less than 20 μm nearest to the electrolyte layer at the anode–electrolyte interface [46]. Carbon deposition over this layer would result in reduced active sites for electrochemical oxidation of the fuel, and then serious deterioration of the cell performance, which may explain the quick deterioration of cell performance for the cell without the catalyst layer when operating on pure methane fuel, as observed in our previous study [31]. The carbon deposition over the anode region near the anode–electrolyte interface would also introduce large internal stress, which may explain the crack formation over the thin-film electrolyte. It is interesting that only a small amount of carbon was deposited inside

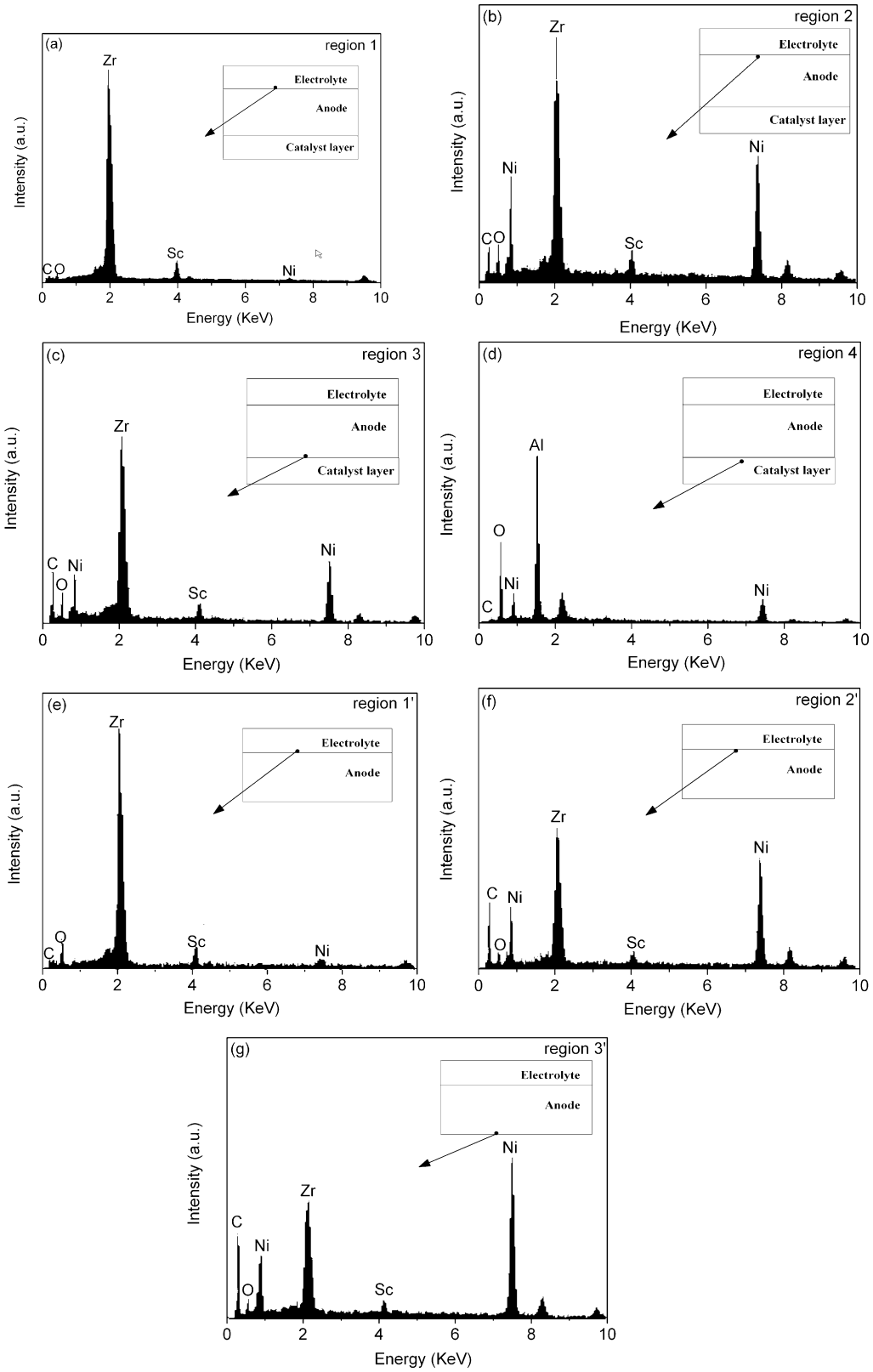


**Fig. 10.** EDX spectra taken from different regions of the cell with (a–d) and without (e–g) the catalyst layer after treatment of pure methane for 5 min.

the Ni–$Al_2O_3$ catalyst layer, which can be explained by the fact that the absolute amount of nickel catalyst in the catalyst layer was very small; the nickel weight percentage in the catalyst layer was only 7 wt.%, while it was about 54 wt.% nickel in the anode.

## 4. Conclusions

The 7 wt.% Ni–$Al_2O_3$ catalyst had excellent catalytic activity, comparable to that of Ru–$CeO_2$ for methane partial oxidation, methane steam reforming and methane $CO_2$ reforming reactions

between 600 and 850 °C. The strong interaction between nickel oxide and the $Al_2O_3$ support and the small crystalline size of the nickel accounted for the high activity of Ni–$Al_2O_3$ catalyst for such reactions. The excellent catalytic activity of Ni–$Al_2O_3$ towards methane steam reforming and methane $CO_2$ reforming resulted in high cell performance when a fuel cell anode with a Ni–$Al_2O_3$ functional layer was operated on methane–$H_2O$ or methane–$CO_2$ gas mixtures. Because of its much better mechanical performance, Ni–$Al_2O_3$ was superior to Ru–$CeO_2$ from the aspect of cell integrity for the applications where repeated thermal cycling or redox cycling are needed, for example, in single-chamber operation mode. As compared to Ru–$CeO_2$, Ni–$Al_2O_3$ did not suppress coke formation, however, the introduction of $CO_2$ and $H_2O$ in methane reduced the coke formation rate considerably. In a real fuel cell, the Ni–$Al_2O_3$ catalyst layer effectively protected the anode from coke formation, especially for the region near to the anode–electrolyte interface, where the electrochemically active sites are mainly located. This is the reason for the improved cell performance when operating on methane fuel when a Ni–$Al_2O_3$ anode catalyst was adopted, as demonstrated in our previous study [31]. The much cheaper price of Ni–$Al_2O_3$ over Ru–$CeO_2$, its excellent catalytic properties and mechanical performance, and its effectiveness in preventing coke formation over the anode layer are promising for its adoption as the anode catalyst layer in solid-oxide fuel cells operating on methane fuel.

## Acknowledgements

This work was supported by the National Natural Science Foundation of China under Contract Nos. 20676061 and 20703024, by the National 863 Program under Contract No. 2007AA05Z133, and by the National Basic Research Program of China under Contract No. 2007CB209704.

## References

[1] K. Scott, E. Yu, G. Vlachogiannopoulos, M. Shivare, N. Duteanu, J. Power Sources 175 (2008) 452–457.
[2] M.C. Williams, J.P. Strakey, S.C. Singhal, J. Power Sources 131 (2004) 79–85.
[3] EG&G Technical Services, Inc. and Science Applications International Corporation, Fuel Cell Handbook, 6th edition, US-DOE/NETL-2002/1179, Morgantown, WV, 2002.
[4] S. Mclntosh, R.J. Gorte, Chem. Rev. 104 (2004) 4845–4865.
[5] M. Mogensen, K. Kammer, Annu. Rev. Mater. Res. 33 (2003) 321–331.
[6] S. Park, J.M. Vohs, R.J. Gorte, Nature 404 (2000) 265–267.
[7] T. Hibino, A. Hashimoto, K. Asano, M. Yano, M. Suzuki, M. Sano, Electrochem. Solid-State Lett. 5 (2002) A242–A244.
[8] T. Hibino, A. Hashimoto, T. Inoue, J. Tokuno, S. Yoshida, M. Sano, Science 288 (2000) 2031–2033.
[9] K. Sasaki, Y. Hori, R. Kikuchi, K. Eguchi, A. Ueno, H. Takeuchi, M. Aizawa, K. Tsujimoto, H. Tajiri, H. Nishikawa, Y. Uchida, J. Electrochem. Soc. 149 (2002) A227–A233.
[10] Q.L. Ma, R.R. Peng, Y.J. Lin, J.F. Gao, G.Y. Meng, J. Power Sources 161 (2006) 95–98.
[11] M.F. Liu, R.R. Peng, D.H. Dong, J.F. Gao, X.Q. Liu, G.Y. Meng, J. Power Sources 185 (2008) 188–192.
[12] Y.Z. Wu, C. Su, C.M. Zhang, R. Ran, Z.P. Shao, Electrochem. Commun. 11 (2009) 1265–1268.
[13] Y.Z. Chen, Z.P. Shao, N.P. Xu, Energy Fuels 22 (2008) 1873–1879.
[14] N. Laosiripojana, S. Assabumrungrat, Appl. Catal. A: Gen. 320 (2007) 105–113.
[15] A. Tomita, S. Teranishi, M. Nagao, T. Hibino, M. Sano, J. Electrochem. Soc. 153 (2006) A956–A960.
[16] T. Hibino, A. Hashimoto, M. Yano, M. Suzuki, M. Sano, Electrochim. Acta 48 (2003) 2531–2537.
[17] H. Kishimoto, K. Yamaji, T. Horita, Y.P. Xiong, N. Sakai, M.E. Brito, H. Yokokawa, J. Power Sources 172 (2007) 67–71.
[18] T. Kim, G. Liu, M. Boaro, S.-I. Lee, J.M. Vohs, R.J. Gorte, O.H. Al-Madhi, B.O. Dabbousi, J. Power Sources 155 (2006) 231–238.
[19] S.H. Clarke, A.L. Dicks, K. Pointon, T.A. Smith, A. Swann, Catal. Today 38 (1997) 411–423.
[20] R.J. Gorte, J.M. Vohs, Curr. Opin. Colloid Interface Sci. 14 (2009) 236–244.
[21] H.P. He, J.M. Vohs, R.J. Gorte, J. Electrochem. Soc. 150 (2003) A1470–A1475.
[22] H. Kim, C. Lu, W.L. Worrell, J.M. Vohs, R.J. Gorte, J. Electrochem. Soc. 149 (2002) A247–A250.
[23] S.W. Tao, J.T.S. Irvine, Nat. Mater. 2 (2002) 320–323.
[24] B. Huang, S.R. Wang, R.Z. Liu, X.F. Ye, H.W. Nie, X.F. Sun, T.L. Wen, J. Power Sources 167 (2007) 39–46.
[25] Y.B. Lin, Z.L. Zhan, J. Liu, S.A. Barnett, Solid State Ionics 176 (2005) 1827–1835.
[26] Y.B. Lin, Z.L. Zhan, S.A. Barnett, J. Power Sources 158 (2006) 1313–1316.
[27] J. Liu, S.A. Barnett, Solid State Ionics 158 (2003) 11–16.
[28] G. Goula, V. Kiousis, L. Nalbandian, I.V. Yentekakis, Solid State Ionics 177 (2006) 2119–2123.
[29] Z.L. Zhan, Y.B. Lin, M. Pillai, I. Kim, S.A. Barnett, J. Power Sources 161 (2006) 460–465.
[30] Z.P. Shao, S.M. Haile, J. Ahn, P.D. Ronney, Z.L. Zhan, S.A. Barnett, Nature 435 (2005) 795–798.
[31] W. Wang, W. Zhou, R. Ran, R. Cai, Z.P. Shao, Electrochem. Commun. 11 (2009) 194–197.
[32] Z.L. Zhan, S.A. Barnett, J. Power Sources 157 (2006) 422–429.
[33] Z.L. Zhan, S.A. Barnett, Science 308 (2005) 844–847.
[34] C.W. Sun, Z. Xie, C.R. Xia, H. Li, L.Q. Chen, Electrochem. Commun. 8 (2006) 833–838.
[35] Z.L. Zhan, S.A. Barnett, Solid State Ionics 176 (2005) 871–879.
[36] Z.L. Zhan, S.A. Barnett, J. Power Sources 155 (2006) 353–357.
[37] Y.Z. Chen, W. Zhou, Z.P. Shao, N.P. Xu, Catal. Commun. 9 (2008) 1418–1425.
[38] W. Zhou, Z.P. Shao, W.Q. Jin, J. Alloys Compd. 426 (2006) 368–374.
[39] H.X. Gu, R. Ran, W. Zhou, Z.P. Shao, J. Power Sources 172 (2007) 704–712.
[40] N.P. Brandon, S. Skinner, B.C.H. Steele, Annu. Rev. Mater. Res. 33 (2003) 183–213.
[41] S. Takenaka, H. Umebayashi, E. Tanabe, H. Matsune, M. Kishida, J. Catal. 245 (2007) 392–400.
[42] S.D. Robertson, B.D. McNicol, H. De Bass, S.C. Kloet, J.W. Jenkins, J. Catal. 37 (1975) 424–431.
[43] S. Xu, R. Zhao, X.L. Wang, Fuel Process. Technol. 86 (2004) 123–133.
[44] Y. Jiang, A.V. Virkar, J. Electrochem. Soc. 150 (2003) A942–A951.
[45] S.P. Chai, S.H.S. Zein, A.R. Mohamed, Diam. Relat. Mater. 16 (2007) 1656–1664.
[46] F. Zhao, A.V. Virkar, J. Power Sources 141 (2005) 79–95.